Available online at www.sciencedirect.com
ScienceDirect
Journal of Power Sources 180 (2008) 423–432
JOURNAL OF POWER SOURCES
www.elsevier.com/locate/jpowsour

Advanced computational tools for PEM fuel cell design Part 2. Detailed experimental validation and parametric study

P.C. Sui [a], S. Kumar [b], N. Djilali [a,*]

[a] *Institute for Integrated Energy Systems and Department of Mechanical Engineering, University of Victoria, Victoria, BC V8W 3P6, Canada*
[b] *Ballard Power Systems, 9000 Glenlyon Parkway, Burnaby, BC V5J 5J8, Canada*

Received 18 December 2007; received in revised form 6 February 2008; accepted 6 February 2008
Available online 14 February 2008

Abstract

This paper reports on the systematic experimental validation of a comprehensive 3D CFD-based computational model presented and documented in Part 1. Simulations for unit cells with straight channels, similar to the Ballard Mk902 hardware, are performed and analyzed in conjunction with detailed current mapping measurements and water mass distributions in the membrane-electrode assembly. The experiments were designed to display sensitivity of the cell over a range of operating parameters including current density, humidification, and coolant temperature, making the data particularly well suited for systematic validation. Based on the validation and analysis of the predictions, values of model parameters, including the electro-osmotic drag coefficient, capillary diffusion coefficient, and catalyst specific surface area are determined adjusted to fit experimental data of current density and MEA water content. The predicted net water flux out of the anode (normalized by the total water generated) increases as anode humidification water flow rate is increased, in agreement with experimental results. A modification of the constitutive equation for the capillary diffusivity of water in the porous electrodes that attempts to incorporate the experimentally observed immobile (or irreducible) saturation yields a better fit of the predicted MEA water mass with experimental data. The specific surface area parameter used in the catalyst layer model is found to be effective in tuning the simulations to predict the correct cell voltage over a range of stoichiometries.

Keywords: Computational fluid dynamics; Modeling; Membrane transport; Water balance; Current mapping; Capillary diffusivity

1. Introduction

A number of reviews have recently provided a status of computational fluid dynamics (CFD) models for PEMFCs [1–4]. One of the main focuses in this paper is the issue of validation. Table 1 summarizes recent modeling and simulation studies on PEMFC and the methods used in validating them. Until recently, most numerical simulations relied on validating computational results by so-called zero-dimensional data such as the *V–I* curve and overall water balance, which are global, spatially averaged values. This approach provides limited confidence, even when the number of data used for validation is abundant; for instance entirely different electric field distributions obtained from simulations in which the electrochemical asymmetry factor is varied can result in essentially identical global polarization curves [5]. Studies using reduced dimensions and simplified models and listed in Table 1, focus on analysis (a) across the MEA [6], (b) along-the-channel [7–13], and (c) under-the-rib [14]. Each approach has its merits in providing physical insights into the transport phenomena in the geometric space considered. The validation with global data such as polarization curves or water balance, however, should be interpreted with caution as there are uncertainties associated with some of the underlying assumptions in the simplified models as well the multi-dimensional effects not considered in the models. When locally resolved data are used for validation [15,16], the same concern remains. The uncertainties due to model simplification and reduced dimensions are obviously relaxed when comprehensive, 3D simulations are employed [17–23], but uncertainties remain due to fitting of global data. More recently, some numerical simulations have been validated against local experimental data [24–26].

* Corresponding author. Tel.: +1 250 721 6034; fax: +1 250 721 6323.
E-mail address: ndjilali@uvic.ca (N. Djilali).

0378-7753/$ – see front matter © 2008 Elsevier B.V. All rights reserved.
doi:10.1016/j.jpowsour.2008.02.008

Nomenclature

C_p	specific heat (J mol^{-1} K^{-1})
D_λ	water diffusion coefficient (mol m^{-1} s^{-1})
I	current density (A m^{-2})
$\dot{m}$	mass flow rate of fluid (kg s^{-1})
n_d	electro-osmotic drag coefficient
P	pressure (Pa)
RH	relative humidity
s	saturation
S/V	specific surface area (m^2 m^{-3})
T	temperature (K)

Greek letter

λ	water content

Subscripts

A	anode side
C	cathode side

In the present study, the comprehensive 3D CFD code described in Part 1 [27] is validated against experimental data obtained for a unit cell. The data include local current density distribution and mass of water along the channel measured over a wide range of operating conditions that results in significant differences in the dominant processes and couplings, making this data set particularly challenging for 3D simulations. The objectives of this paper are two-fold: first, validation of the physical models and some determination of model parameters from the experimental data set, and, second, parametric analysis to gain insight into the extent and effects of salient transport processes.

2. Methodology

2.1. Experimental data

The experimental data used for validation were collected using the MRED (MEA Resistance and Electrode Diffusion) method developed by Stumper et al. [28]. This method allows *in situ* determination of MEA resistance and electrode diffusivity of the cell. The anode and cathode surfaces of the unit cell are attached to 16 current collector pucks, which connect to the electrical load. The current through each puck is determined by the voltage drop across a shunt resistor on each puck. The test cell is operated on a custom-designed test station allowing accurate control and monitoring of all operating parameters. Steady-state polarization curves are obtained under constant fuel and oxidant stoichiometry with respect to the total current.

The mass of water in the MEA is determined using a non-destructive method that measures the weight of water *ex situ*. The mass of the water is measured individually for each of the 16 pucks to provide the water distribution for the MEA. Experimental data are collected for a range of operating conditions. These data are used to validate the model predictions by post-processing the 3D CFD predictions in exactly the same manner as in the experiments. Post-processing of the 3D fields is described in Part 1 [27].

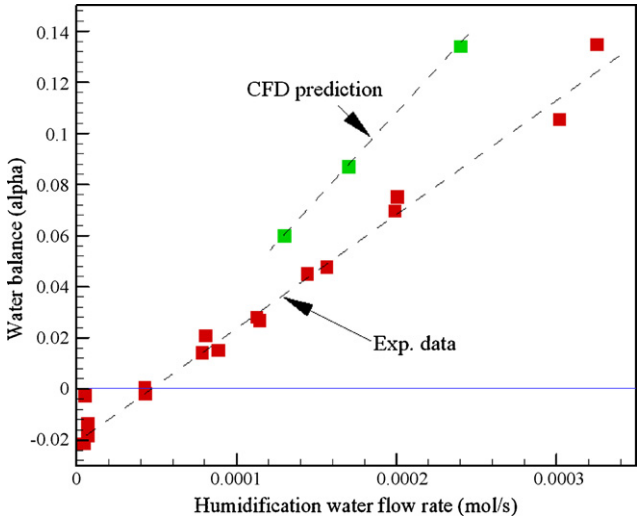

Fig. 1. Comparison of water balance data and numerical predictions.

3. Results and discussion

3.1. Water balance: numerical versus experimental

Water balance, defined as the net water transfer between the anode inlet and outlet normalized by the total water generated by the cell, is a measurable quantity that characterizes water management of a unit cell. A negative value indicates a net transfer from anode to cathode. As far as validation of numerical simulations is concerned, the water balance is a zero-dimension integral quantity, and should therefore be interpreted with caution regarding local water transfer across the membrane inside the unit cell, in particular for a counter-flow configuration when water may diffuse from cathode to anode. Fig. 1 shows a comparison

Table 1
Summary of literature on numerical simulation and validation

Model	Data used for validation	
	Global data: V–I, water balance	Local data: I, T, y_i, m_w
Reduced dimension, simplified model	Bernardi and Verbrugge [6], Gurau and Liu [7], Yi and Nguyen [8], Rowe and Li [9], You and Liu [10], Siegel et al. [11] and Kulikovsky [15]	Berg et al. [13] and Kulikovsky [15]
Comprehensive, 3D	Um and Wang [16], Dutta et al. [17][a], Zhou and Liu [18], Berning and Djilali [19][a], Lee et al. [20][a], Mazumder and Cole [21], Li and Becker [23] and Sivertsen and Djilali [5]	Ju and Wang [24] and Li and Becker [23]

[a] The membrane was not spatially resolved in the computation.

Table 2
Summary of experimental conditions for CFD input

Case	Nominal specs	I (A cm^{-2})	Cathode				Anode			
			DP,ox (C)	Tox,in (C)	RH	stoich	DP,h2 (C)	Th2,in (C)	RH	stoich
1	Baseline	1.0	62.0	65.9	0.839	1.66	54.4	74.2	0.411	1.50
2	RH50%	1.0	52.3	65.1	0.549	1.71	38.4	73.9	0.185	1.54
3	RH25%	1.0	37.2	65.3	0.252	1.76	56.7	68.3	0.590	1.52
4	RH0%	1.0	0.0	65.4	0.026	1.78	57.0	62.3	0.782	2.24
5	I = 0.45	0.45	62.3	65.3	0.874	1.66	54.7	74.9	0.405	1.50
6	I = 0.1	0.1	62.7	64.5	0.924	2.82	54.5	74.5	0.408	1.50
7	Stoich = 1.6	1.0	61.9	65.5	0.849	1.48	54.1	75.0	0.390	1.51
8	Stoich = 1.4	1.0	61.7	64.7	0.873	1.29	31.9	75.4	0.122	1.57
9	Stoich = 1.2	1.0	61.9	65.1	0.865	1.11	0.0	75.3	0.017	1.59

Pressure at inlet: $P_A = 3.2$ bar, $P_C = 3.0$ bar.

of water balance versus anode humidification water flow rate for the baseline case with different anode inlet dew point temperatures. The average current density is 1 A m^{-2} for all cases shown. Both experiments and predictions show a linear variation of water balance with anode humidification water flow rate. Under dryer anode conditions, the experimental data shows negative water balance, suggesting back diffusion from the cathode side.

3.2. Compilation of MEA water mass data

Experimental data obtained by the MRED method for a unit cell are used in the present investigation. The test conditions are summarized in Table 2. The MRED data basically consist of water content profiles and current mapping data for unit cell operated under various operating conditions. To illustrate the broad range of operating conditions over which the data was taken, Fig. 2 shows all MEA water mass data plotted versus current density for the 13 test cases listed in Table 2. Two observations from this figure are: (a) water content of the MEA populates the range of 5 ± 0.5 mg cm^{-2}—this is considered as a "saturated MEA", corresponding to a fully humidified membrane and a partially saturated GDL having a maximum saturation of ca. 0.2, cf. Appendix A and (b) low current density results correlate to low water content, suggesting that low current density conditions might be associated with relatively higher ohmic resistance in the MEA. The broad range of operating conditions documented experimentally make this data set particularly useful in assessing the performance of the model over a large operating envelope with different dominant and/or limiting transport mechanisms.

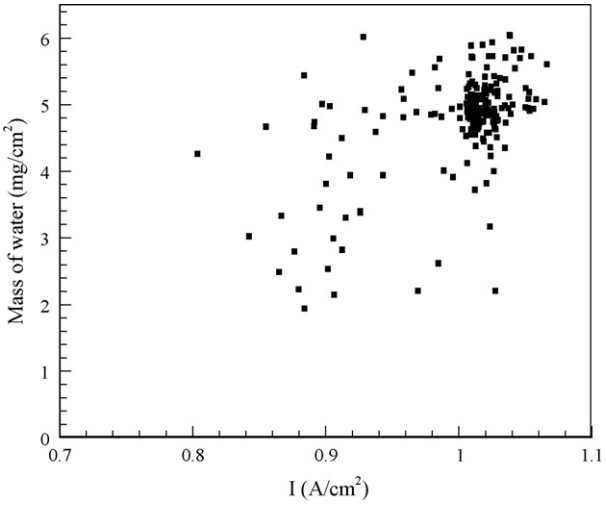

Fig. 2. Compilation of 13 cases of MRED data.

3.2.1. Sensitivity to inlet humidification

Fig. 3 shows a comparison of experimental data versus CFD baseline results for four humidification cases, i.e. RH for 84, 55, 25 and 0.03%, respectively. One can see that the numerical results are consistent with experimental data qualitatively for different humidification but there are quantitative discrepancies between them. The numerical predictions fail to show the saturated MEA region in the middle of the cell. The drop off of water content in the cathode outlet (high puck number) appears to be more pronounced in the data than numerical prediction.

Several attempts of adjusting the MEA properties are taken to fit the data: (1) capillary diffusion coefficient used for porous media, (2) membrane properties including the sorption isotherm, drag coefficient and water diffusivity, and (3) specific surface area in the cathodic catalyst layer. Comparison and analysis of numerical prediction versus experimental data are given in the following sections.

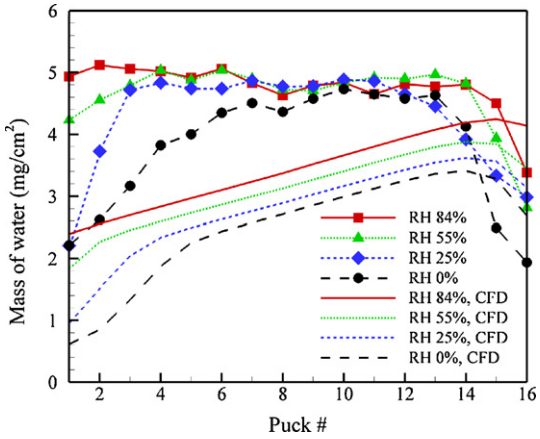

Fig. 3. MEA water content profiles: experimental data versus CFD baseline.

3.3. Capillary diffusion coefficient

The rationale in changing the capillary diffusion coefficient is that a number of porous media exhibit an immobile or critical saturation value (also referred to as irreducible saturation) below which the effective capillary diffusion is zero. Very recent pore network simulations targeted at GDL media exhibit critical saturation values in the range of 0.1–0.2 [29,30]. This is consistent with the inference from the results that the default capillary diffusion coefficient appears to high, thus resulting in lower than observed water retention in the GDL. A numerical experiment was thus performed to investigate the effects of capillary diffusion coefficient on predicted GDL water content.

Fig. 4 shows a comparison of the default and modified correlations for the capillary diffusion coefficient. The modified correlation tested here has a trend similar to the default and is represented by two segments over the range $s = [0,1]$, but the overall values are lower than in default correlation. The formula for the tested case takes an exponential form:

$$D_{\text{cap}} = A \cdot [\exp(ks) - 1] \quad (1)$$

For $s \leq 0.2$, $A = 10^{-5}$, $k = 57.6$; for $s > 0.2$, $A = 10^{-2}$, $k = 5.77$. The low saturation region in the tested correlation has a region of very low value to mimic the immobile regime for water. Fig. 5 shows the predicted mass of water using the hypothetical correlation of capillary diffusion coefficient for the same cases presented in Fig. 3. One can see that the mass of water in the middle portion is shifted up to be closer to the experimental data, while on both ends of the cell the discrepancies remain. It is noted that the boundary dividing the single-phase regime and two-phase regime is not affected by the correlation used for capillary diffusion coefficient.

The effects of capillary diffusion coefficient can be seen in Fig. 6, which shows a more diffuse distribution of saturation in the GDL using the default correlation. With reduced value of capillary diffusion coefficient, water generated in the catalyst layer tends to remain in the GDL until the saturation approaches 0.2. Owing to the low saturation condition in the gas channel, the saturation in the GDL hardly exceeds 0.2 because the liquid leaves the GDL readily once this threshold value is attained.

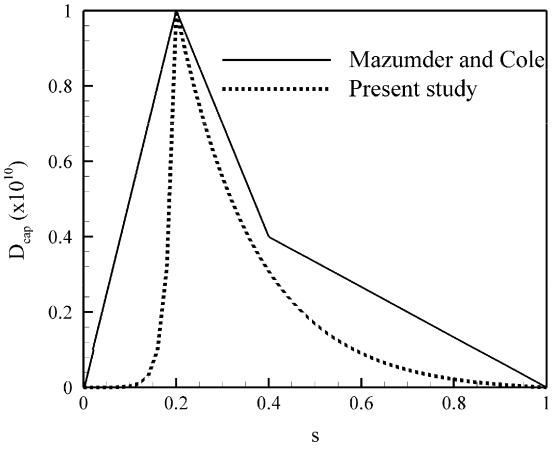

Fig. 4. Capillary diffusion coefficient used in the calculation.

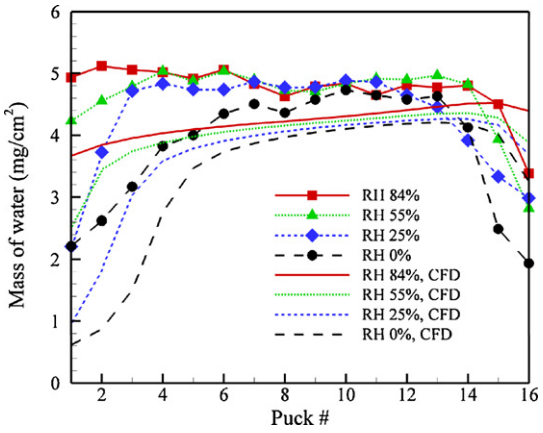

Fig. 5. Comparison of experimental data and numerical predictions using the user Dcap correlation for capillary diffusion coefficient.

Therefore the second half of the correlation for capillary diffusion coefficient (for $s > 0.2$) does not play a role in the numerical prediction.

Fig. 7(a) and (b) shows the current density profiles of experimental data and numerical predictions using different correlation of capillary diffusion coefficient. The discrepancy in the current density prediction is obvious for low humidification cases (RH 25% and RH 0% cases). One can see for the cases tested, that the capillary diffusion coefficient, or rather the transport of liquid water, has little impact on current density predictions. It should be noted that the sensitivity to RH in the experiments is mostly confined to the inlet/outlet regions and this is not entirely surprising as such counterflow anode/cathode arrangements can promote humidification via internal water recirculation as described by Büchi and Srinivasan [31].

3.4. Membrane properties

3.4.1. Parametric study: EOD

In order to assess the impact of the electro-osmotic drag coefficient, a parametric study is undertaken, and the results are shown in Fig. 8. The diffusion coefficient for water in the membrane was maintained constant (1.2×10^{-12} m^2 s^{-1}), while the drag coefficient, $n_d = (n_d^*/22)\lambda$, was varied for n_d^* from a value of 2.5 given by Springer et al. [32] to one order magnitude smaller. It should be noted that a n_d^* value of unity was reported by Zawodzinski et al. [33] and used in simulation by some researchers, e.g. Berg et al. [13]. As the EOD is decreased, less water is dragged from anode to cathode near the cathode inlet, whereas near the anode inlet more water diffuses across the membrane from cathode to anode. This results in better membrane humidification near the cathode inlet, and hence a higher current density, see Fig. 9. A lower current density region results near the anode inlet, and overall reducing the EOD yields predicted current density profiles that deviate more from experimental data.

3.4.2. Sorption isotherm

The predicted water mass in the MEA obtained with various models is compared to measurements in Fig. 10. The

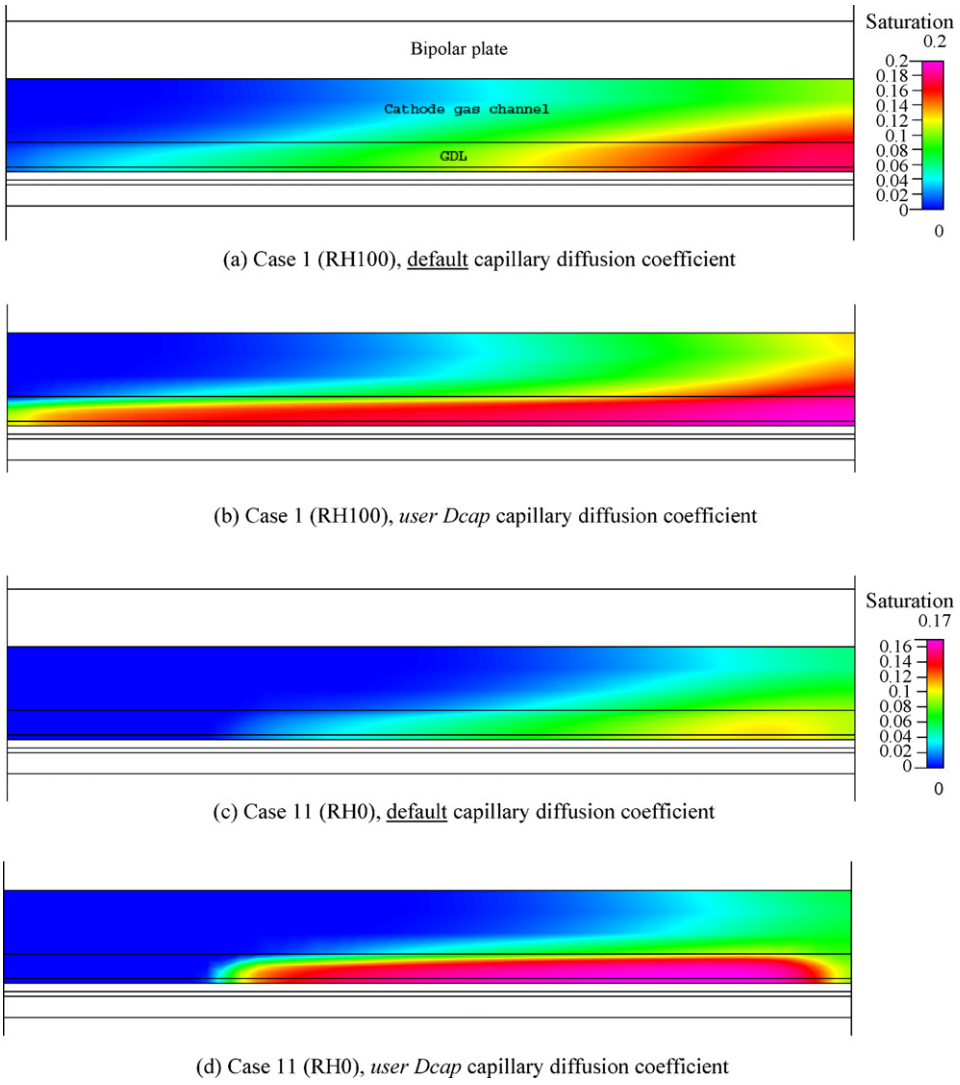

Fig. 6. Predicted saturation in the cathode side of the MEA and gas channel. (a) Case 1 (RH100), default capillary diffusion coefficient, (b) Case 1 (RH100), *user Dcap* capillary diffusion coefficient, (c) Case 11 (RH0), default capillary diffusion coefficient, (d) Case 11 (RH0), *user Dcap* capillary diffusion coefficient.

predicted water mass plotted with triangles is calculated using the original sorption isotherm given in Springer et al. [32]; the square symbols represent predictions using a modified sorption isotherm that has a smooth transition over $\lambda = 14$–22 to near unity water activity to account for the different water content value between vapor and liquid water equilibrated states (i.e. the so-called Schroeder's paradox). The predicted mass of water in the membrane phase is essentially constant except for a drop near the anode inlet due to the low RH in the anode channel. The amount of liquid water, resulting mainly from water condensation in the cathode side, increases along the channel and slightly near the anode inlet due to back diffusion as discussed earlier. The experimental data falls between the predictions using the Springer isotherm and the modified isotherm. Fig. 11 shows a comparison of predicted current density profiles using different sorption isotherms with experimental data. Unlike the case for MEA water mass, the current density prediction using Springer's isotherm yields a closer match to the experimental data.

From the exercise with the capillary diffusion coefficient, it is found that the computed water content in the *inlet* region is always lower than measured data. It is then reasonable to consider possible non-equilibrium effects in the membrane at low humidity conditions. Sorption isotherms are obtained by equilibrating the membrane over a sufficiently long period of time with water vapor of known RH. It is speculated that an equilibrium state might not be reached for low humidity conditions in an operating fuel cell. Therefore, a heuristic approach is taken to illustrate how non-equilibrium effects can impact the predictions of water content and current density profiles. Fig. 12 shows the default sorption isotherm for Nafion used in the calculation versus an hypothetical correlation having a parabolic form.

Fig. 13 shows predicted water content profiles using different sorption isotherms. For the "non-equilibrium" isotherm, one can see an increase in water content prediction, particularly in the inlet region. This, however, shows a gap between the numerical prediction and data. If one shifts the prediction curve up to make the plateau region of the curve to be 5 mg cm^{-2}, the inlet

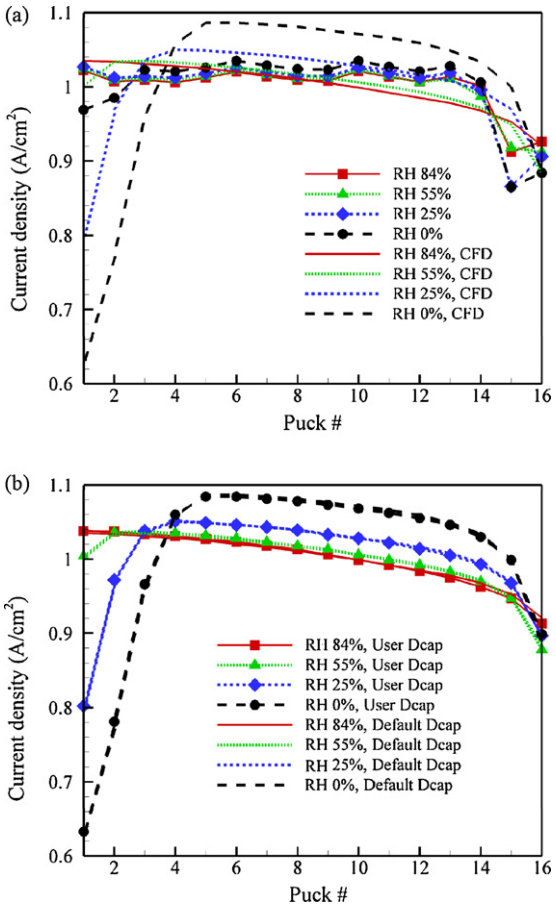

Fig. 7. Comparison of predicted current density profiles with experimental data (a) CFD versus experimental data (b) Predicted current density profile using default and *user Dcap* (marked as UserDcap in legend) correlation for capillary diffusion coefficient.

region of the water content compares closely to experimental data, whereas the cathode outlet portion of the curve shows a large discrepancy. The drop-off of water content in cathode outlet shown in experimental data may be simulated by lowering the coolant flow rate as will be discussed later. The use of the "non-equilibrium" sorption isotherm yields a more satisfactory

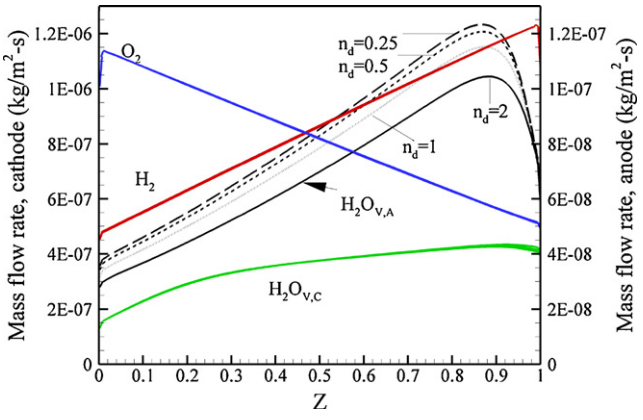

Fig. 8. Numerical predictions of mass flow rate with different EOD coefficient values.

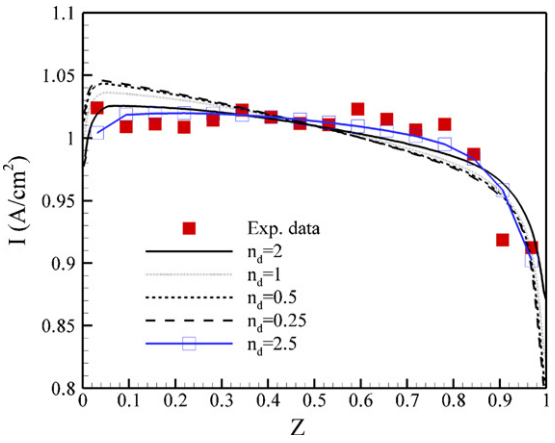

Fig. 9. Comparison current density data with numerical predictions for different EOD coefficient values.

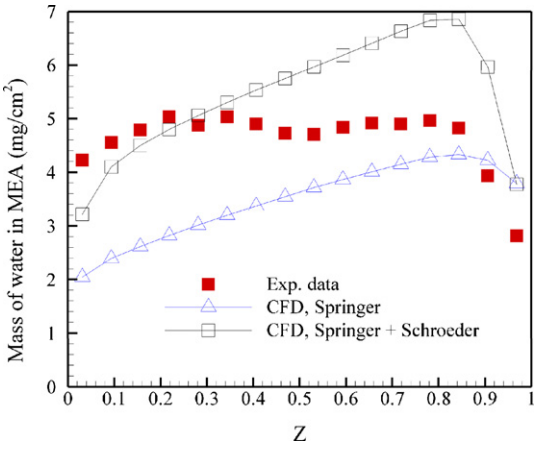

Fig. 10. Comparison of data of water mass in the MEA with numerical predictions.

result in current density prediction than in water content profile, cf. Fig. 13.

3.4.3. *Water diffusivity in membrane*

For the sake of simplicity, the water diffusivity in the membrane is fixed at 1.2E−10 $m^2\ s^{-1}$ for most of the calculations in

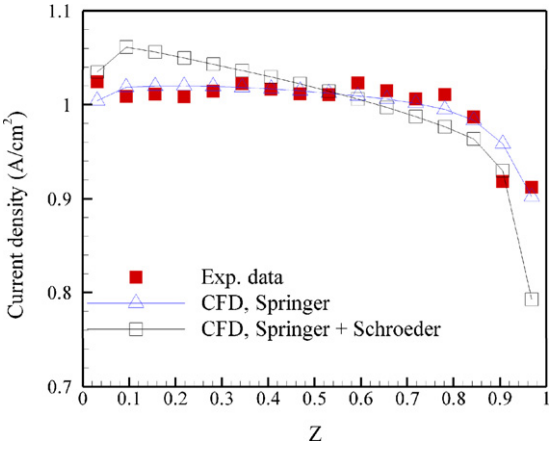

Fig. 11. Comparison of current density data with numerical predictions.

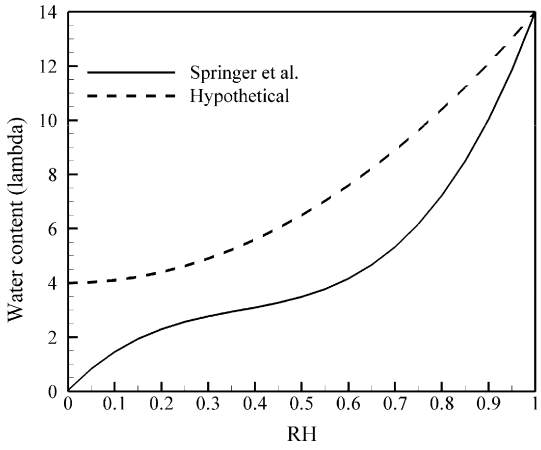

Fig. 12. Sorption isotherms used in calculation; Nafion = default, artificial = hypothetical correlation.

the present study, which differs from that given in Springer et al. [32]. This value is indeed close to the diffusivity corresponding to an activity of unity in the original Springer paper. Fig. 14(a) and (b) shows that the difference in predicted water content and current density using the constant diffusivity and the correlation of Springer et al. is not significant.

3.5. Catalyst layer

3.5.1. Specific surface area for fitting stoichiometry sensitivity data

The stoichiometry sensitivity of a unit cell is important for fuel cell stack operation because in a stack the cells are likely to operate at different stoichiometric ratios and minimum loss in performance due to unevenly distributed stoichiometric ratio is desired. Therefore, in addition to the single cell performance, the stoichiometry sensitivity is an important measure of a unit cell. As the stoichiometric ratio approaches unity, performance of the cell decreases due to mass transfer limitation, which can occur at different region of the unit cell, e.g. in the GDL due to liquid water blockage or in the catalyst layer due to pore level mass diffusion. The effects due to mass transfer through the GDL

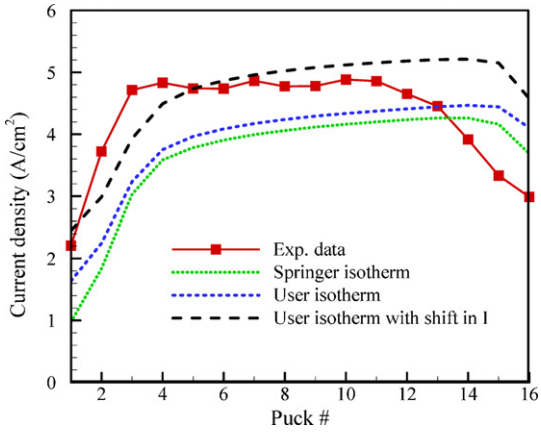

Fig. 13. Water content predictions using different sorption isotherms and average pore size.

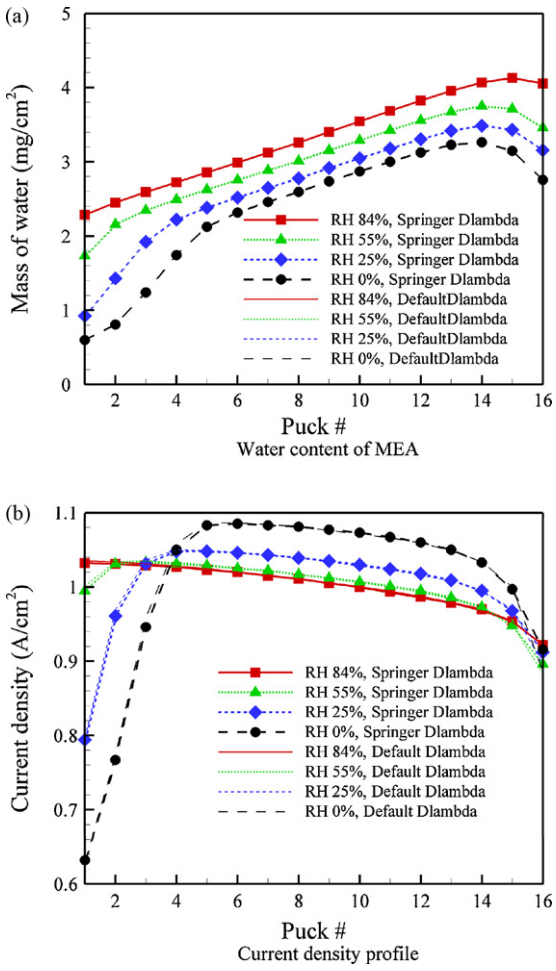

Fig. 14. Comparison of water content and current density predictions using a constant water diffusivity in membrane and the Springer model: (a) water content of MEA and (b) current density profile.

manifest in the saturation transport, which has been included in the aforementioned tests. The pore-level mass transfer in the catalyst layer is treated via the so-called "diffusion-reaction balance," cf. [21,27]. The model parameter used to fit experimental data of stoichiometric sensitivity is the specific surface area (S/V) of the catalyst. Fig. 15 shows a comparison of data of cell voltage with numerical predictions using S/V ranging from 2 to 100. It is found that the value $S/V = 3$ fits the data best.

3.5.2. On the limiting current predicted using the current CFD model

The limiting current for a unit cell is dependent on many factors along the pathway of oxidant transfer. From the gas channel inlet to the catalyst surface, transfer of oxygen is subjected to limiting mechanisms including (a) oxygen concentration gradient along the channel due to local consumption, (b) convective mass transfer from the channel bulk flow to the GDL surface, (c) diffusive transfer through the GDL in the presence of porous solid and liquid water, (d) dissolution of oxygen into water and electrolyte, (e) diffusion of oxygen in the and mass diffusion in the pore level, and (f) diffusion of dissolved oxygen in the electrolyte. In the current CFD model for PEMFC, factors (a),

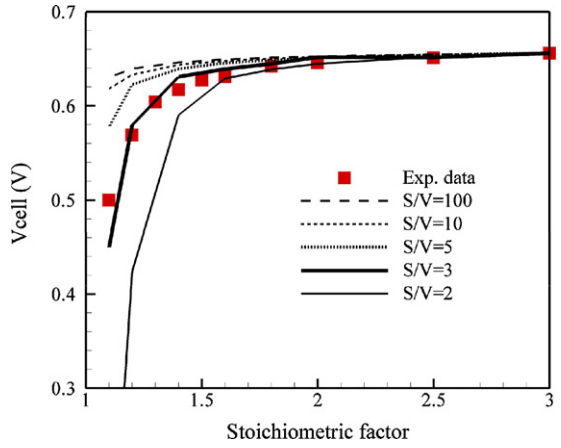

Fig. 15. Predicted cell voltage as a function of oxygen stoichiometric ratio with various *S*/*V* (sov in the legend) values.

(b), (c) are included in the simulation. Contribution by factors (d) and (f) are not explicitly modeled, however, both factors can be lumped into the reaction-diffusion balance (e), and can be handled by one control parameter, e.g. the specific surface area of catalyst *S*/*V*. Ultimately the transport processes that have not been accounted for should be modeled as more experimental data and analysis become available.

To gain insight into the limiting current change due to the model parameter *S*/*V*, a series of polarization curve predictions are calculated for various stoichiometric factors for two oxygen concentrations. Fig. 16 shows a comparison of the numerical results. The stoichiometric factor is calculated based on air at $I = 1\ \mathrm{A\,cm^{-2}}$. The stoichiometric ratio (*stoich* in Fig. 16) of these cases is adjusted by changing the inlet gas velocity; e.g. for stoich = 1.1, the inlet gas velocity is 1.1 times the inlet velocity required for an average current density of $1\ \mathrm{A\,cm^{-2}}$ when air is used. The cases with high oxygen concentration has the oxygen and nitrogen concentration swapped for air. For the air cases,

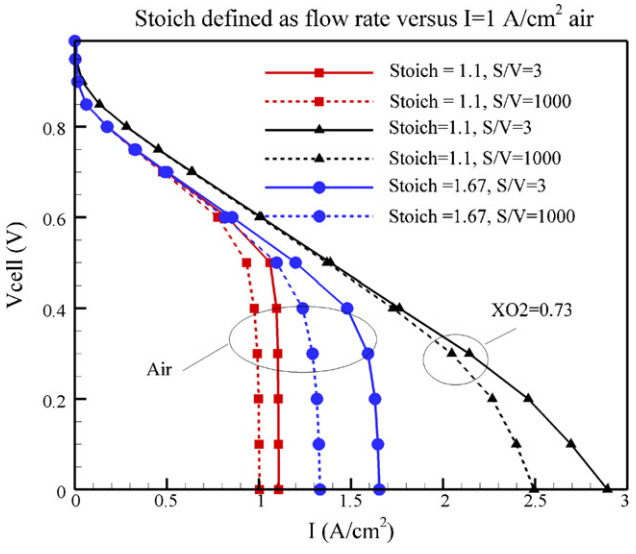

Fig. 16. Predicted polarization curves with various oxygen flow rates and concentrations. The oxygen stoichiometric factor is based on using air at $I = 1\ \mathrm{A\,cm^{-2}}$.

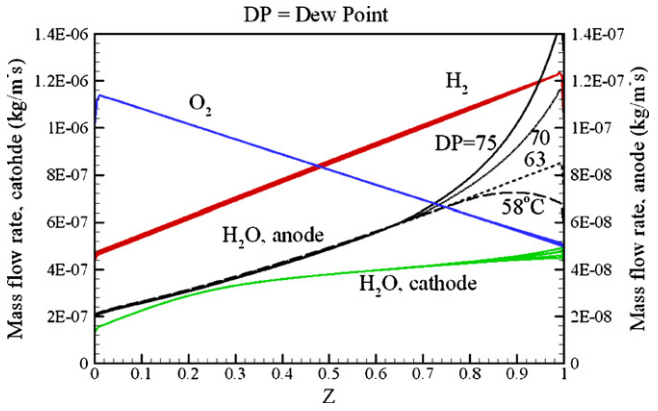

Fig. 17. Numerical predictions of mass flow rate for different anode humidification.

the limiting current when a high *S*/*V* is used coincides with the stoichiometry of oxygen. When *S*/*V* = 3 is used, which provides the best fit for stoichiometry sensitivity data, the limiting current shifts to a lower value than the high *S*/*V* case. For the higher oxygen concentration cases, zero cell potential occurs prior to the limiting current condition. It should be noted that for the cases with high oxygen concentration ($X_{O_2} = 0.73$ in Fig. 16), the amount of oxygen flow rate at inlet is in fact equivalent to stoich = 3.46 based on air because of the high oxygen concentration at the inlet. The implication of this study is that one may use limiting current data to calibrate the model parameter used for the reaction-diffusion balance.

3.6. Operating conditions

3.6.1. Anode humidification

Fig. 17 shows the flow rates for four different anode humidification conditions corresponding to inlet dew point temperatures of 58, 63, 70, and 75 °C. The only noticeable difference is in the anode water vapor flow, which exhibits a monotonic decrease along the channel except for the drier case (58 °C dew point). It is interesting to note that near the anode outlet the water vapor flow rates all converge to a similar level. The cases shown in Fig. 18 are calculated with the same potential difference across the unit cell. The effect due to anode humidification is there-

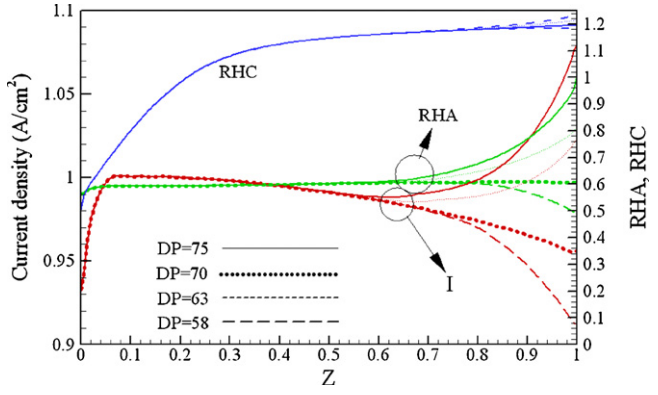

Fig. 18. Numerical predictions of current density and relative humidity for different anode humidification.

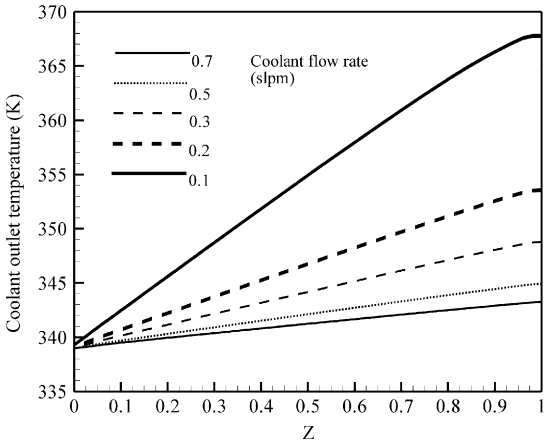

Fig. 19. Predicted coolant temperature profiles in the axial direction for various coolant flow rates.

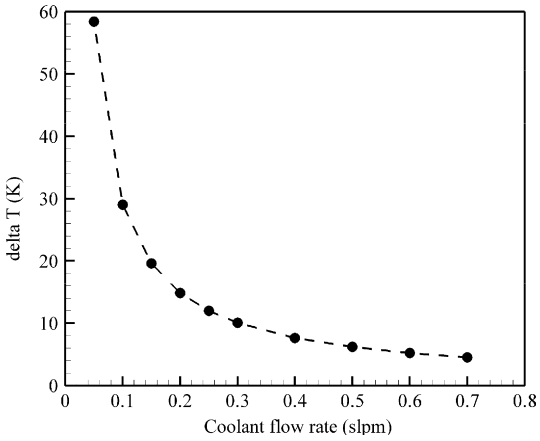

Fig. 21. Temperature difference between coolant inlet and outlet at various coolant flow rates.

fore reflected in the change of local current density near the anode inlet as shown in Fig. 18, which increases with anode humidification.

3.6.2. *Dependence of current density and water content predictions on coolant flow rate*

In comparing the simulation results with experimental data, the coolant flow rate needs to be adjusted in order to obtain temperature gradient in the axial direction similar to that recorded in the experiments because of uncertainty issue in actual experiment operation. Fig. 19 shows the temperature profiles in the axial direction as a function of inlet coolant flow rate. As the coolant flow rate is reduced, the temperature profiles rise and temperature gradient between coolant inlet and outlet becomes higher. The temperature difference between coolant inlet and outlet is shown in Fig. 20. The sensitivity of the cell performance appears to change drastically when the coolant flow rate is reduced to certain point, cf. ca. 0.1 slpm. Similar to stoichiometry sensitivity, the cell performance is also sensitive to coolant flow rate, or rather the heat removal capacity defined as $\dot{m}C_p$. As is show in Fig. 21, once the heat removal capacity drops below certain threshold value, the cell performance will be significantly reduced. Such condition may occur when good flow

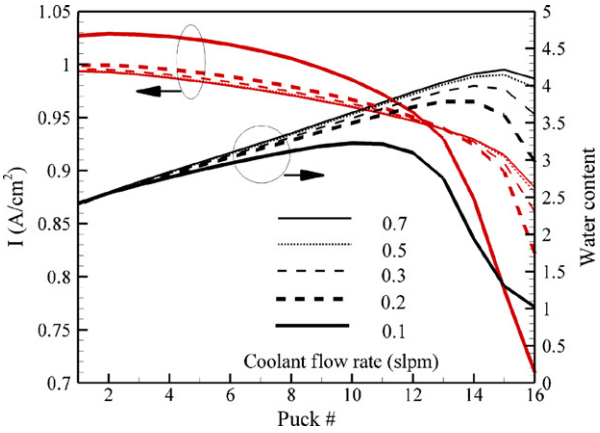

Fig. 20. Predicted water content and current density profiles for various coolant flow rates.

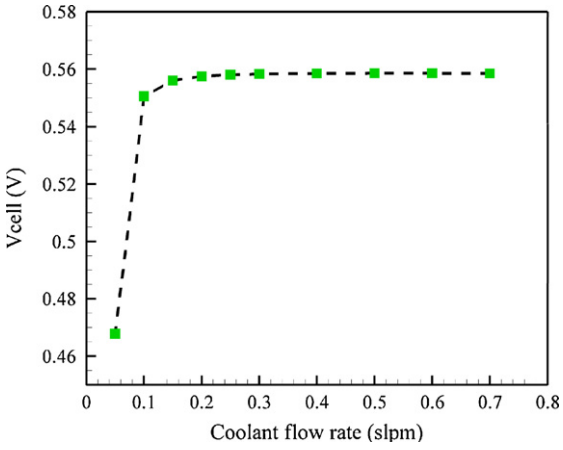

Fig. 22. Predicted cell voltage as a function of coolant flow rate.

sharing of the coolant in a stack is not maintained. Fig. 22 shows the predicted water profiles and current density profiles at various coolant flow rates. When the coolant flow rate is low, the high temperature near the coolant outlet (located on the same side as the cathode gas outlet in the MRED configuration) causes membrane dry-out and an expansion of the low water content region near the outlet.

4. Conclusions

The CFD-based computational framework described in Part 1, was in this paper systematically validated against spatially resolved measurements, including water balance and current density distributions, obtained under a broad range of operating conditions that stretch the computational model in general, and the embedded constitutive relations of some of the sub-models in particular. While simulation results based on membrane properties reported by Springer et al. [32] capture the overall trends, examination of the predicted water mass in the MEA using various formulations, show that experimental data is bracketed by predictions using the "standard" sorption isotherm correlation and predictions using a modified correlation that takes into consideration liquid equilibrated conditions.

Based on the analysis, adjustments were proposed for some of the constitutive equations, including the capillary diffusion coefficient for liquid saturation and sorption isotherms for water uptake as well as model parameters such the specific surface area. These adjustments were quite effective in improving the overall fit between experiments and simulations. In the limit of low RH conditions, it is found that adjustments in the coolant flow rate are required to achieve a good fit with experimental with respect to water content in the cathode outlet region. In terms of water transport across the membrane, the cathode outlet region (diffusion-dominated) might differ from the cathode inlet region (drag-dominated) in the direction of net water flux. It is nonetheless possible to identify some critical parameters that yield a good fit of the water content profile at both ends of the cell simultaneously, indicating capabilities to account for a large range of changes in terms of dominant transport mechanisms and a level of generality that is promising in terms of functionality for design. The extensive validation undertaken here would further benefit from experimental method that could accurately differentiate water content in the GDL from that in the membrane. Finally, it is clear that fundamental studies are required to set some of the constitutive relations and correlations on firmer ground. Some very recent developments for characterizing the two-phase flow in gas diffusion media [29,30,34] have resulted for instance in new capillary and relative permeability functions that should further enhance the reliability and generality of computational fuel cell models.

Acknowledgements

Funding for this work was provided to ND by the MITACS Network of Centres of Excellence and Ballard Power Systems. The authors wish to acknowledge the insightful inputs of Jason Chisham, Ryan Mackie, Radu Bradean and John Kenna throughout this work. Thanks are also due to Jürgen Stumper and Michael Löhr for providing the experimental data, and to ESI-CFD for the technical assistance of Ning Zhou and the provision of CFD ACE+ software licenses.

Appendix A. Sample calculation for the mass of water in the MEA

For a GDL of 250 μm in thickness and porosity 0.6, and a membrane of 50 μm.

- For a saturation of 0.2 in the GDL, the water content is $250\text{E}{-6}\,\text{m} \times 0.6 \times 0.2 \times 1000\,\text{kg}\,\text{m}^{-3} \times 1\text{E}6\,\text{mg}\ \text{kg}^{-1} \times 1\text{E}{-4}\ \text{m}^2\,\text{cm}^{-2} = 3\,\text{mg}\ \text{cm}^{-2}$.
- For a fully humidified membrane, the water content is $\lambda \times 50\text{E}{-6}\,\text{m} \times 1980\,\text{kg}\,\text{m}^{-3}{-}1.1\,\text{kg}\ \text{mol}^{-1} \times 0.018\,\text{kg}\ \text{mol}^{-1} \times 1\text{E}6\,\text{mg}\ \text{kg}^{-1} \times 1\text{E}{-4}\ \text{m}^2\,\text{cm}^{-2} = 0.162\lambda\,\text{mg}\ \text{cm}^{-2}$.
- For $\lambda = 14$ (vapor-equilibrated), the value of water content is about $2.3\,\text{mg}\,\text{cm}^{-2}$ and $3.6\,\text{mg}\,\text{cm}^{-2}$ for $\lambda = 22$ (liquid-equilibrated).

References

[1] A.Z. Weber, J. Newman, Chem. Rev. 104 (10) (2004) 4679–4726.
[2] D. Cheddie, N. Munroe, J. Power Sources 147 (1/2) (2005) 72–84.
[3] K.W. Lum, J.J. McGuirk, J. Electrochem. Soc. 152 (4) (2005) A811–A817.
[4] N. Djilali, Energy 32 (4) (2007) 269–280.
[5] B.R. Sivertsen, N. Djilali, J. Power Sources 141 (1) (2005) 65–78.
[6] D.M. Bernardi, M.W. Verbrugge, J. Electrochem. Soc. 139 (9) (1992) 2477–2491.
[7] V. Gurau, H.T. Liu, S. Kakac, AIChE J. 44 (11) (1998) 2410–2422.
[8] J.S. Yi, T.V. Nguyen, J. Electrochem. Soc. 145 (4) (1998) 1149–1159.
[9] A. Rowe, X.G. Li, J. Power Sources 102 (1/2) (2001) 82–96.
[10] L.X. You, H.T. Liu, Int. J. Heat Mass Transfer 45 (11) (2002) 2277–2287.
[11] N.P. Siegel, M.W. Ellis, D.J. Nelson, M.R. von Spakovsky, J. Power Sources 115 (1) (2003) 81–89.
[12] A.A. Kulikovsky, J. Electrochem. Soc. 150 (11) (2003) A1432–A1439.
[13] P. Berg, K. Promislow, J. St Pierre, J. Stumper, B. Wetton, J. Electrochem. Soc. 151 (3) (2004) A341–A353.
[14] A.A. Kulikovsky, J. Divisek, A.A. Kornyshev, J. Electrochem. Soc. 146 (11) (1999) 3981–3991.
[15] A.A. Kulikovsky, Electrochem. Commun. 6 (12) (2004) 1259–1265.
[16] S. Um, C.Y. Wang, K.S. Chen, J. Electrochem. Soc. 147 (12) (2000) 4485–4493.
[17] S. Dutta, S. Shimpalee, J.W. Van Zee, Int. J. Heat Mass Transfer 44 (11) (2001) 2029–2042.
[18] T.H. Zhou, H.T. Liu, J. Power Sources 138 (1/2) (2004) 101–110.
[19] T. Berning, N. Djilali, J. Electrochem. Soc. 150 (12) (2003) A1589–A1598.
[20] W.K. Lee, S. Shimpalee, J.W. Van Zee, J. Electrochem. Soc. 150 (3) (2003) A341–A348.
[21] S. Mazumder, J.V. Cole, J. Electrochem. Soc. 150 (11) (2003) A1503–A1509.
[22] S. Mazumder, J.V. Cole, J. Electrochem. Soc. 150 (11) (2003) A1510–A1517.
[23] S. Li, U. Becker, ASME Fuel Cell Science, Proceedings of the Second Engineering and Technology Conference, Rochester, NY, 2004.
[24] H. Ju, C.Y. Wang, J. Electrochem. Soc. 151 (11) (2004) A1954–A1960.
[25] S. Li, J. Cao, W. Wangard, U. Becker, ASME Fuel Cell Science, Proceedings of the Third Engineering and Technology Conference, Ypsilanti, MI, 2005.
[26] G. Luo, H. Ju, C.Y. Wang, J. Electrochem. Soc. 154 (3) (2007) B316–B321.
[27] P.C. Sui, S. Kumar, N. Djilali, J. Power Sources 180 (2008) 410–422.
[28] J. Stumper, H. Haas, A. Granados, J. Electrochem. Soc. 152 (4) (2005) A837–A844.
[29] J.T. Gostick, M.W. Fowler, M.A. Ioannidis, M.D. Pritzker, Y.M. Volfkovich, A. Sakars, J. Power Sources 156 (2) (2006) 375–387.
[30] B. Markicevic, A. Bazylak, N. Djilali, J. Power Sources 171 (2) (2007) 706–717.
[31] F.N. Büchi, S. Srinivasan, J. Electrochem. Soc. 144 (8) (1997) 2767–2772.
[32] T.E. Springer, T.A. Zawodzinski, S. Gottesfeld, J. Electrochem. Soc. 138 (8) (1991) 2334–2342.
[33] T.A. Zawodzinski, T.E. Springer, J. Davey, R. Jestel, C. Lopez, J. Valerio, S. Gottesfeld, J. Electrochem. Soc. 140 (7) (1993) 1981–1985.
[34] E.C. Kumbur, K.V. Sharp, M.M. Mench, J. Electrochem. Soc. 154 (12) (2007) B1295–B1304.